A New Look at Deformation as a Diagnostic for Large-Scale Flow

CLEMENS SPENSBERGER AND THOMAS SPENGLER

Geophysical Institute, University of Bergen, Bergen, Norway

ABSTRACT

Deformation plays a key role in atmospheric dynamics because it provides a dynamical measure of the interaction between different scales, such as in frontogenesis. A climatology of deformation constructed from Interim ECMWF Re-Analysis (ERA-Interim) data (1979–2013) reveals four main processes associated with deformation: 1) frontogenesis at lower levels, 2) movement and evolution of jet streams in the upper troposphere, 3) orographic blocking, and 4) Rossby wave breaking. The merits of deformation as an additional perspective are discussed for these processes on the basis of case studies and composite analyses in conjunction with analytic solutions.

This study shows that deformation can be used to unambiguously detect orographic blocking through the local strength of the flow diversion around orography. Moreover, the deformation signature for orographic blocking observed in case studies and composites closely resembles the analytic solution for two-dimensional flow around an obstacle.

The climatology also reveals that Rossby wave breaking is associated with a characteristic γ-shaped deformation maximum. A composite analysis of this process confirms previous findings that suggested a dynamic link between Rossby wave breaking and dynamic blocking. It is shown that the deformation associated with Rossby wave breaking is aligned with the observed mean deformation upstream and downstream of a blocking high. Therefore, the presented composites illustrate a potential mechanism pinpointing how Rossby wave breaking can act to reinforce the flow diversion around the block.

1. Introduction

Shearing and stretching deformation are regularly employed for analysis of mesoscale flow evolution, whereas mainly vorticity and its divergence forcing are utilized for analysis on larger scales. At the mesoscale, the primary use of deformation is for frontal kinematics because deformation is one of the most important ingredients for frontogenesis or frontolysis (Petterssen 1936; Keyser et al. 1988). Bishop and Thorpe (1994), Renfrew et al. (1997), and Chaboureau and Thorpe (1999) showed how deformation on the frontal scale can feed back on the synoptic scale by influencing the development of frontal waves and secondary cyclogenesis. At larger scales, Vuorela (1953) tried to relate the skill of forecasts based on the barotropic vorticity equation to the deformation field. However, he concluded that ''deformation seemed to be of the same order of

magnitude in all cases investigated here and more or less unorganized'' Vuorela (1953, p. 415). With the advent of global high-resolution reanalysis products, we are now in a position to revise this rather discouraging conclusion. We demonstrate that deformation carries significant and valuable information when investigating large-scale circulation patterns, such as orographic and dynamic blocking as well as Rossby wave breaking.

A potential reason for the inconsiderable usage of deformation on larger scales lies in the nature of the equations that we mainly use to diagnose and predict the flow evolution on these scales, namely, the potential vorticity equation in its barotropic, shallow water, and quasigeostrophic (QG) approximations (e.g., Vallis 2006). In these approximations, the flow is dominated by its rotational component, and it is only stretching of absolute vorticity that needs to be assessed in order to make a prediction. Hence, large parts of the dynamical link with the mesoscale are neglected. However, as the magnitude and vertical structure of fronts depend on this link, the observed frontal configurations during the life cycle of cyclones (e.g., Bjerknes 1919; Shapiro and Keyser 1990) are generally more diluted in these formulations.

Corresponding author address: Clemens Spensberger, Geophysical Institute, University of Bergen, Allegt. 70, 5007 Bergen, Norway.
E-mail: clemens.spensberger@gfi.uib.no

Other approximations, such as semigeostrophic theory, retain more of the dynamical links between the large-scale and mesoscale flow (Hoskins 1975). Here, also, the ageostrophic flow can steepen synoptic-scale gradients through deformation in the mesoscale frontal circulation. The deformation of the ageostrophic flow can thus add valuable information on the interaction between the synoptic-scale cyclone and the mesoscale front.

Deformation has also been used to study filamentation and the associated enstrophy cascade in two-dimensional turbulence (Okubo 1970; Charney 1971; Weiss 1991). Filamentation denotes a process, similar to frontogenesis, in which the length scale of a gradient reduces gradually until the gradient can be removed via dissipation, thereby identifying the location of mixing. A typical large-scale process associated with mixing of potential vorticity (PV) on isentropic surfaces is the breaking of Rossby waves, where Rossby wave breaking is viewed as the irreversible overturning of PV contours on isentropic surfaces (McIntyre and Palmer 1983; Thorncroft et al. 1993; Appenzeller et al. 1996; Rivière and Orlanski 2007). Most Rossby wave breaking detection algorithms are contour based, thus only giving an indication if an overturning exists or not (e.g., Wernli and Sprenger 2007; Strong and Magnusdottir 2008; Rivière 2009). Deformation, however, can add quantitative information by directly reflecting the strength of filamentation as one of the underlying processes.

LaPeyre et al. (1999) derived a criterion for the conditions under which gradients align with the deformation axis of dilatation, using the strength of deformation as a key ingredient. Such an alignment not only reorients a gradient but also strongly increases the efficiency of deformation-driven frontogenesis. As the PV gradient determines the position, orientation, and strength of the jet stream (e.g., Hoskins et al. 1985; Davies and Rossa 1998), deformation in conjunction with the condition by LaPeyre et al. (1999) provides a framework to describe jet stream dynamics, including Rossby wave breaking events. This framework renders deformation a crucial stepping stone that facilitates further analysis and understanding of what leads to the overturning of PV gradients. The potential of this perspective has been demonstrated by Rivière and Joly (2006a,b), Rivière (2008), and Oruba et al. (2013), who studied the dynamical implications of common distributions of the Okubo–Weiss criterion in low-frequency flow.

In addition to Rossby wave breaking, deformation also indicates flow diversion, which is present in flow around a body of stagnant air, for example, during dynamic or orographic blocking. Thus, deformation might provide a diagnostic to clarify the processes behind a proposed dynamical link between Rossby wave
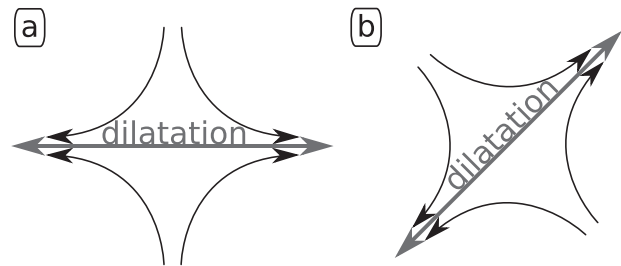

FIG. 1. Principal flow patterns (black arrows), and associated axis of dilatation (black double arrows) for (a) stretching deformation and (b) shearing deformation.

breaking and dynamic blocking (e.g., Berrisford et al. 2007; Altenhoff et al. 2008). Furthermore, deformation has a significant advantage in diagnosing topographic blocking compared to conventional methods, such as the Froude number or the nondimensional mountain height (e.g., Smith 1979; Ringler and Cook 1997), because deformation relies only on the instantaneous flow in the proximity of the topography. In contrast, the aforementioned conventional methods are based on approximations of the mean conditions of flow and stratification upstream of the obstacle. These approximations usually introduce a certain arbitrariness in the diagnosis and thus limit the generality of these methods. Moreover, combining deformation due to topographic effects and frontal dynamics can help to further test ideas on the interaction between fronts and topography (e.g., Egger and Hoinka 1992, and references therein).

In this study, we illustrate the additional perspective and value that deformation can provide for different large-scale atmospheric processes, such as dynamic and topographic blocking, as well as Rossby wave breaking. The theoretical background is given in section 2. The methods and data used are laid out in section 3. In section 4, we present analytic solutions and composites derived from the Interim European Centre for Medium-Range Weather Forecasts Re-Analysis (ERA-Interim) data. We give our concluding remarks in section 5.

2. Theoretical background

The gradient of the horizontal velocity vector $\mathbf{u} = (u, v)$ can be partitioned into vorticity $\zeta = v_y - u_x$, divergence $D = u_x + v_y$, stretching deformation $\delta_+ = u_x - v_y$, and shearing deformation $\delta_\times = u_y + v_x$, where subscripts x and y denote partial derivatives in the respective directions (e.g., Batchelor 1967). The principal flow patterns associated with pure stretching or shearing deformation are shown in Fig. 1. The axis of dilatation is the axis along which an initially square parcel is stretched, indicated by black double arrows. The two flow patterns in Fig. 1 differ only by a rotation of $+45°$
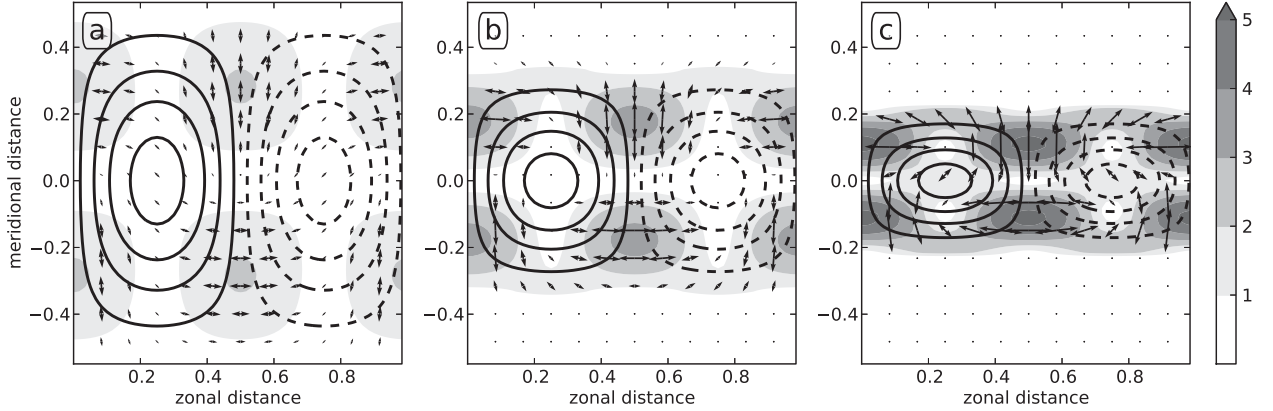
FIG. 2. Deformation associated with an idealized Rossby wave train for different aspect ratios $\alpha \in \{(5/8)\sqrt{2}, \sqrt{2}, (8/5)\sqrt{2}\}$. The shading and the length of the double arrows indicate total deformation, and orientation of the double arrows depicts the orientation of the axis of dilatation. Contours represent the nondimensionalized streamfunction with a contour interval of 7.5×10^{-3} centered around zero. Negative contours are dashed.

and are otherwise identical. A rotation of 90° reverses the arrows and hence inverts the sign of the respective deformation component. A rotationally invariant measure of the strength of deformation is the total deformation

$$\delta \equiv \sqrt{\delta_+^2 + \delta_\times^2}, \qquad (1)$$

and the angle of deformation γ contains the information about the orientation of the deformation, where

$$\gamma \equiv \frac{1}{2} \arctan \frac{\delta_\times}{\delta_+} \qquad (2)$$

is defined as the angle between the x axis and the axis of dilatation.

The names and notations for deformation differ within the literature. For example, LaPeyre et al. (1999) refer to total deformation as strain and denote it as σ. They also use ϕ as a measure similar to the angle of deformation, but define it relative to the $y = x$ line rather than the x axis. In contrast, publications on frontogenesis generally define the angle of deformation relative to the orientation of the gradient in question (e.g., Keyser et al. 1988). Furthermore, these publications often denote this angle with β instead of γ. We do not follow this convention to avoid confusion with $\beta = f_y$, the meridional variation of the Coriolis parameter.

Deformation associated with Rossby wave trains

To shed some light on characteristic features of deformation associated with Rossby waves, we consider a homogeneous basic state and a streamfunction anomaly of the form

$$\psi' = \psi_0' \sin\hat{x} \cos^2\left(\frac{\alpha}{2}\hat{y}\right), \qquad (3)$$

for $\alpha\hat{y} \in [-\pi, \pi]$. The horizontal coordinates $\hat{x}, \hat{y}$ are nondimensionalized by the horizontal length scale L, yielding $(\hat{x}, \hat{y}) = L^{-1} 2\pi(x, y)$. Therefore, the only free parameters are the aspect ratio $\alpha = L/L_y$ and the perturbation amplitude ψ_0', where L_y is the meridional perturbation length scale.

Using the geostrophic streamfunction, the deformation components become

$$\delta_{+g}' = -2\psi_{xy}' = \alpha\psi_0' \cos\hat{x} \sin\alpha\hat{y}; \qquad (4)$$

$$\delta_{\times g}' = \psi_{xx}' - \psi_{yy}' = \frac{\psi_0'}{2}[(\alpha^2 - 1)\cos\alpha\hat{y} - 1]\sin\hat{x}. \quad (5)$$

The deformation associated with the Rossby wave train is partly asymmetric with respect to the $\hat{x}$ axis, even though the geopotential anomalies are symmetric (Fig. 2). Mathematically, the asymmetry in the angle of deformation is introduced by $\psi_{xy} = v_y$ in Eq. (4), which is antisymmetric with respect to the $\hat{x}$ axis. In contrast, total deformation is symmetric with respect to the $\hat{x}$ axis and independent of the sign of the geopotential anomaly because total deformation only depends on the flow speed and the magnitude of the curvature of the streamlines, which are both independent of the sign of the anomaly.

The areas of strong streamline curvature are much more confined than the geopotential anomaly. Accordingly, the horizontal length scale of deformation is smaller compared to the length scale of the streamfunction. The strongest deformation appears in the confluent and diffluent regions of the meridional wind
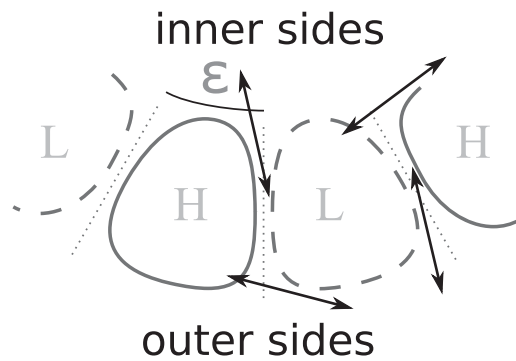
FIG. 3. Schematic of a curved Rossby wave train and its associated deformation. Owing to the bend, the inner side is compressed, decreasing the radius of the geopotential isolines. Simultaneously, the angle by which the wind is turned on the inner side is decreased by ϵ. On the outer side, the opposite happens: both the radius and the turning angle increase.

anomalies. In the confluent regions, the axis of dilatation points toward the meridional wind maximum because confluent zonal winds turn meridionally into these regions. In contrast, in diffluent regions where the meridional wind turns zonally, the deformation is oriented zonally as well.

The symmetry of the geopotential anomalies neither allows for zonal wind along the $\hat{x}$ axis nor for a meridional gradient of the meridional wind. Hence, all deformation that appears at the center of the geopotential anomalies in Figs. 2a and 2c must be shearing deformation, and the sign and strength of deformation depends on the aspect ratio of the wave. The critical aspect ratio is $\sqrt{2}$, as the term in square brackets in Eq. (5) changes sign at that point. For zonally elongated waves ($\alpha^2 \gg 2$), the u_y shear dominates the v_x shear, and vice versa for meridionally elongated waves ($\alpha^2 \ll 2$). At the critical aspect ratio, the contributions from u_y and v_x cancel each other in the center of the anomaly, resulting in zero deformation (Fig. 2b).

If the wave train is curved positively, the inner sides of the depicted geopotential anomalies are compressed in the zonal direction compared to a straight wave train (Fig. 3). The compression leads to a smaller curvature radius of the streamlines, and hence stronger deformation, because deformation is inversely proportional to the curvature radius for a given wind speed. As a consequence, the area-integrated deformation is proportional to the area-integrated curvature, which is a measure for the total change in flow direction. This total change in geostrophic flow direction, however, decreases on the inner sides by the angle ϵ (Fig. 3) such that the average deformation on the inner side must decrease. Analogous arguments apply for the outer sides in Fig. 3 and the case of a negatively curved wave train.

3. Data and methods

Our analysis is based on 6-hourly ERA-Interim data (Dee et al. 2011), where we calculate the total deformation δ and the angle of deformation γ for the time period 1979–2013. The provided data are interpolated to 0.5° in latitude and longitude. We present case studies and composites to illustrate the different processes associated with deformation. The composites are constructed for either deformation or geopotential values above the 99th percentile at a given location and refer to the boreal winter season [December–February (DJF)]. We present the composite mean of the total deformation δ and the most frequent angle of deformation γ. The most frequent angle is determined from histograms of the angle of deformation with a binning interval of 5°.

The numerical robustness of this method decreases with reduced amounts of data on which the histogram is based. However, the main features of the histogram, such as the most dominant orientation of the axis of dilatation, are retained down to approximately monthly statistics with a sample size of around 120 composite members.

We restrict our presentation to 800 and 300 hPa. The 800-hPa level constitutes a trade-off between a concurrent proximity to low-level frontogenesis and to peak altitudes of major mountain ranges to account for orographic blocking. We choose 300 hPa for the upper troposphere because the jet streams are most pronounced at this level. We tested the sensitivity of our choices by varying the levels by ±100 hPa, revealing that our discussion and conclusions are qualitatively insensitive to our choice of pressure levels (not shown).

4. Processes associated with deformation

a. Cyclone evolution

1) CASE STUDY

The case study in Fig. 4 illustrates the deformation associated with an explosively developing cyclone (Sanders 1986). The cyclone starts to develop on 25 January 1984 close to Newfoundland as a secondary cyclone to a preexisting trough over northeastern Canada. The main signature of deformation in Fig. 4 is associated with fronts. The frontal configurations closely follow the life cycle of an ideal cyclone, as described by Shapiro and Keyser (1990). The third frontal structure pointing toward the northwest in Fig. 4a is a reactivated front from the preexisting trough. During the course of the event, the front becomes incorporated in the bent-back front.

As deformation reflects sharp gradients in wind speed and direction across the frontal boundary, the deformation bands in Fig. 4 closely follow the fronts.
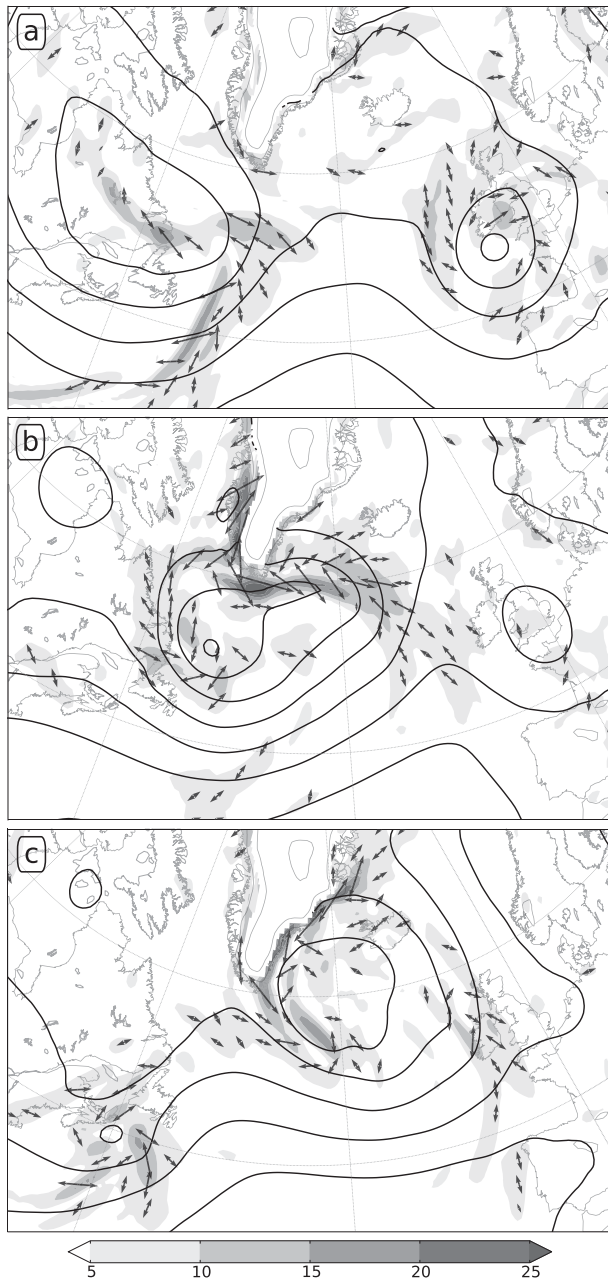
FIG. 4. Case study of a rapidly developing cyclone over New-foundland interacting with the steep orography of southern Greenland. Shading indicates the strength of deformation in units of $10^{-5}\,\mathrm{s}^{-1}$. Contours denote geopotential with a contour interval of $1000\,\mathrm{m}^2\,\mathrm{s}^{-2}$. Panels show the development from (a) 1200 UTC 26 Jan in 24-h intervals to (b) 1200 UTC 27 Jan and (c) 1200 UTC 28 Jan 1984. The case is taken from Sanders (1986), who investigated several cases of explosive cyclogenesis in the eastern North Atlantic.

Furthermore, deformation can act frontogenetically, thus providing a measure for the activeness of a front (Petterssen 1936). The relation between the activeness of the front and the cyclone development is apparent in
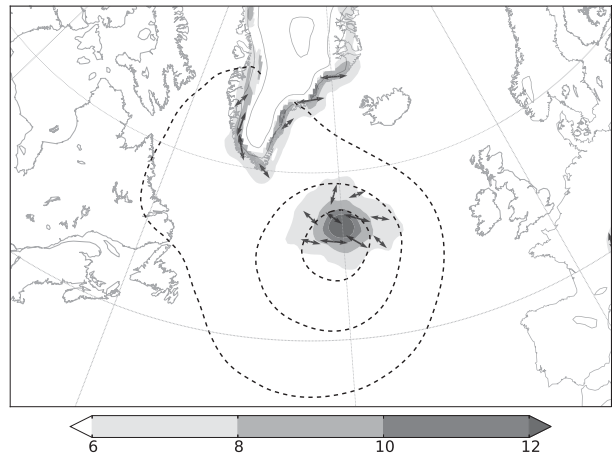

FIG. 5. Composite of cases with deformation above the 99th percentile at 800 hPa at 55°N, 30°W in the winter months DJF. The shading depicts the strength of deformation exceeding $4 \times 10^{-5}\,\mathrm{s}^{-1}$ with a contour interval of $2 \times 10^{-5}\,\mathrm{s}^{-1}$. The contours indicate the geopotential anomalies associated with those cases. The contour interval is $500\,\mathrm{m}^2\,\mathrm{s}^{-2}$ centered around zero; negative anomalies are dashed.

the evolution of the developing cyclone and the cyclone close to the British Isles, where the strength of the deformation develops in conjunction with the strength of the cyclone.

2) COMPOSITES

Following the example above, we present a composite analysis to show that strong deformation over flat topography is generally associated with developing cyclones. As an example, deformation above the 99th percentile at a position in the center of the Atlantic is associated with a cyclonic geopotential anomaly slightly to the southwest of the strongest total deformation (Fig. 5). The anomaly persists through the entire troposphere, and its westward tilt with height resembles the Eady (1949) model of baroclinic instability (not shown). We repeated the analysis with several points at different latitudes in the Atlantic and Pacific sector, and the results were qualitatively similar.

In addition to the deformation associated with the cyclone, orographic features, such as Greenland or the Alps, also appear as areas with enhanced deformation in Fig. 5. These areas are not associated with the cyclonic anomaly itself but rather with the mean state in winter (not shown).

Compared to the horizontal scale of the cyclone, the deformation maximum is spatially rather confined. As the deformation field of a cyclone is dominated by its fronts, the 99th percentile criterion implicitly requires a front to pass the selected point. In the composite average, the fronts with their different orientations yield a singular peak with an average across-front horizontal
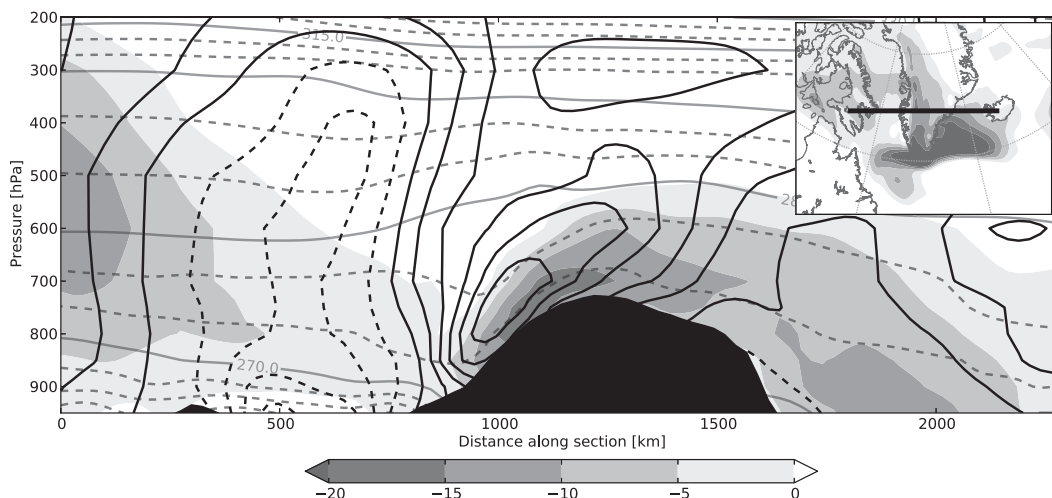
FIG. 6. Cross section through southern Greenland (solid line in inset) at 1200 UTC 27 Jan 1984, corresponding to Fig. 4b. Shading depicts negative u velocities with a contour interval of $5\,\mathrm{m\,s^{-1}}$, gray contours indicate potential temperature (K), and the black contours are v velocities in $5\,\mathrm{m\,s^{-1}}$ intervals centered around zero.

length scale. The different horizontal scales qualitatively follow theory. Assuming the streamfunction perturbation ψ' to be a superposition of waves with horizontal wavenumbers k and l, the relation

$$\delta' = \sqrt{4\psi_{xy}'^2 + \psi_{xx}'^2 + \psi_{yy}'^2 - 2\psi_{xx}'\psi_{yy}'} \propto K^2\psi', \quad (6)$$

where $K^2 \equiv k^2 + l^2$, shows that smaller-scale streamfunction perturbations are associated with stronger deformation perturbations and vice versa.

b. Orographic blocking

1) CASE STUDY

Returning to the case study of the explosively developing cyclone (Fig. 4), the strongest deformation occurs in Figs. 4b and 4c, where parts of the developing cyclone's bent-back front interact with the orography of Greenland. The deformation is concentrated in a narrow band around the orographic obstacle, where the axis of dilatation is generally orientated parallel to the isolines of the orography. This signature in the deformation field is consistent with flow being diverted around blocking orography.

As indicated by the band of deformation, the diverted flow along the east coast of Greenland in Fig. 4c is concentrated in a narrow band along the orography. The highest wind speeds are concentrated in a shallow layer reaching about as high as Greenland's orography (not shown). The structure of the flow with the limited vertical and horizontal extent is very similar to the climatological barrier jet constructed by Harden et al. (2011) for the box they call Denmark Strait South

(DSS). Compared to the barrier jets observed during the Greenland Flow Distortion Experiment (e.g., Petersen et al. 2009), we find no sharp gradients in the thermal structure in our case (not shown), which might be a consequence of the ERA-Interim tending to blur the thermal structure of barrier jets (Harden et al. 2011). Nevertheless, the overall thermal structure in our case with a temperature minimum directly at the coastline is again very similar to the DSS climatology.

Whereas there is also some indication of flow diversion to the south of Greenland by the double arrow at Greenland's tip in Fig. 4b, the orientation of deformation differs within the area of strongest deformation slightly to the south. In that area, the deformation is oriented about 45° with respect to the geostrophic flow, indicating that wind shear is predominant. This shear is set up by strong easterly flow that is reminiscent of the structure of a reverse-tip-jet event as defined by Moore and Renfrew (2005).

Along Greenland's west coast there are additional deformation maxima that are unrelated to orographic blocking but with similar signature and strength (Fig. 4b). Those maxima cannot be explained by orographic blocking because flow that was diverted around the obstacle would be confluent in the lee of blocking orography. This confluence would result in the axis of deformation being oriented perpendicular to the isolines of the orography, whereas they are oriented parallel in the presented case. Figure 6 indicates that the strong deformation in the lee is associated with a downslope windstorm in the lee of Greenland that is deflected to the north by the Coriolis force; this flow is generally called "shooting flow" (e.g., Ball 1956; Durran

1986). Although the deflection leads to a deformation signature resembling orographic blocking, it can only occur downstream of blocking orography. Thus, the different location around the blocking orography allows us to easily differentiate between these processes.

2) ANALYTIC SOLUTION

To better understand the features evident in deformation related to orographic blocking, we briefly discuss the stationary solution for two-dimensional flow around an obstacle. This solution will also be of help when discussing dynamic blocking later on. Lamb (1895) derived such a solution for a spherical obstacle with radius R in polar coordinates (r, φ), where

$$\psi = -u_0 \left(1 - \frac{R^2}{r^2} \right) r \sin \varphi \qquad (7)$$

is the streamfunction of the nondivergent flow and u_0 is the speed of the undisturbed flow approaching from $\varphi = 180°$. Using the relation between streamfunction and deformation [Eq. (A4), see appendix], the total deformation for this solution yields

$$\delta = \frac{4R^2}{r^3} u_0, \qquad (8)$$

showing that the strength of deformation is axisymmetric (Fig. 7). On the windward side, the deformation is oriented parallel to the blocking surface, resembling the flow diversion around Greenland in Figs. 4b and 4c. Along the northern and southern sides of the obstacle, the deformation is dominated by shear, consistent with the deformation pattern close to the southern tip of Greenland (Fig. 4b). On the leeward side, however, the analytic solution differs considerably from the observed patterns. The analytic solution predicts confluent flow that leads to equally strong deformation oriented perpendicular to the block, which is not observed in the case study. Nevertheless, the analytic solution captures the localization and orientation of deformation upstream and to the side of a block remarkably well.

3) COMPOSITES

The case study and analytic solution show that orographic blocking is concurrent with strong deformation concentrated along orography. However, the case study also highlights that orographic blocking is not the only process with such a signature in the deformation field, as shooting flow bears similar features. This poses the question whether orographic blocking is the dominant process associated with the signature in deformation in the vicinity of orography.
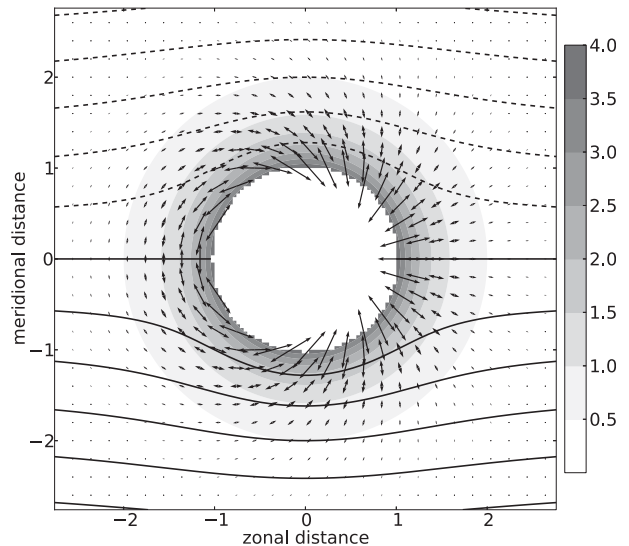

FIG. 7. Stationary solution for 2D flow past a circular obstacle. The shading and double arrows denote deformation analogous to Fig. 2. All variables are normalized with respect to the radius of the circle and the undisturbed flow speed. The contours show streamfunction with a contour interval of 0.5.

To answer this question, we compile composites for deformation above the 99th percentile for a location at the east coast of southern Greenland (Fig. 8a) and a location close to the western slopes of the Alps (Fig. 8b), both at 800 hPa. In both cases, a cyclonic anomaly is associated with flow against the respective slopes. The axes of dilatation are aligned with the isolines of the orography, indicating blocking and resembling the analytic solution and the case study (Figs. 7, 4c). Hence, orographic blocking appears to be the dominant process leading to strong deformation in locations with close proximity to orography.

Both geopotential anomalies in the composites in Fig. 8 are cyclonic. There are, however, situations in which the interaction of an anticyclonic anomaly with orography also induces enhanced deformation. A prominent example is a large anticyclone situated between Iceland and the British Isles. The anticyclone features northerly flow on its western flank, a synoptic pattern that was studied in-depth during the Fronts and Atlantic Storm Track Experiment (FASTEX) campaign (e.g., Petersen et al. 2003). These northerly winds can be blocked by Greenland's south cape, resulting in deformation that can be equally strong as in the cyclonic composites (not shown).

c. Rossby wave breaking

1) CASE STUDY

In the upper atmosphere, deformation is mainly associated with the large wind shear on each side of the jet
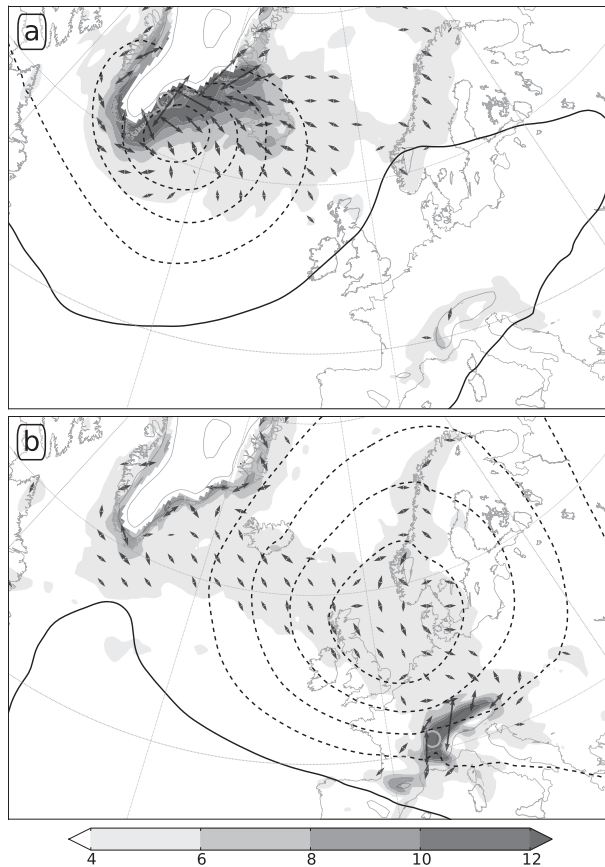
FIG. 8. Composite of cases with deformation above the 99th percentile at 800 hPa at (a) the east coast of Greenland and (b) the western slopes of the Alps in the winter months DJF. The location is indicated by light gray circles. In both cases the cyclonic anomaly is associated with flow against the slopes. Shading and contours as in Fig. 5.
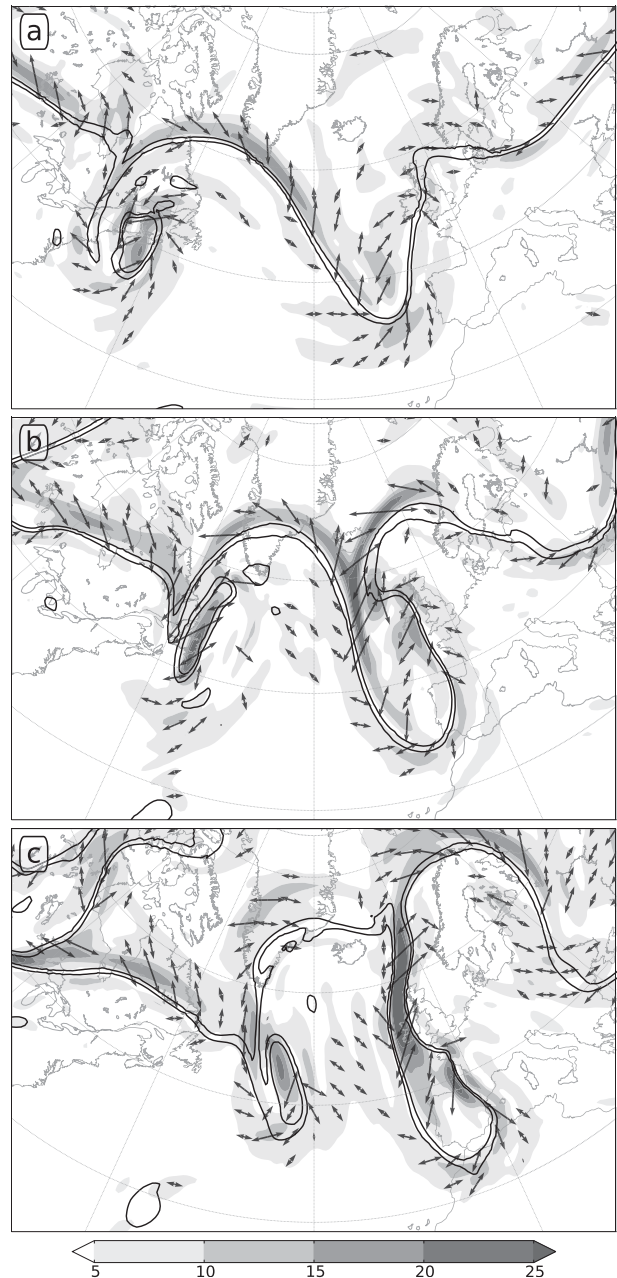

FIG. 9. Case study of a Rossby wave breaking event over western Europe on the $\theta = 315$ K isentropic surface. Shading and arrows are as in Fig. 4. Contours denote the 1- and 2-PVU isolines of potential vorticity. Panels show the development from (a) 0000 UTC 3 Nov, to (b) 0000 UTC 4 Nov, to (c) 0000 UTC 5 Nov 1994. The case is taken from Massacand et al. (1998).

maximum, with deformation following the undulations of the jet accordingly (Fig. 9). For climatological jets, Black and Dole (2000) documented the same shear-dominated pattern. If an undulation becomes steep enough, the wind field features a southward and a northward jet on the two flanks of the undulation. As the zonal scale of this undulation collapses, the wind shear of the two jets superposes, leading to extreme deformation between these two jet streams. This collapse reflects Rossby wave breaking, as it is synonymous to a PV anomaly being deformed into a PV streamer. Massacand et al. (1998) investigated several cases of Rossby wave breaking linked to extreme precipitation along the southern slope of the Alps. The case shown in Fig. 9 is called "Piedmont," after the region that was struck by the most intense precipitation.

On 3 November 1994, the tropopause, represented by the 2 potential vorticity unit (PVU; 1 PVU = 10^{-6} K kg^{-1} m^2 s^{-1}) isoline, features an undulation that is oriented almost meridionally (Fig. 9a). The jet stream closely follows the tropopause, with the axis of dilatation being oriented close to 45° relative to the tropopause on both the tropospheric and stratospheric side, indicating pure shearing deformation in a coordinate system rotated along the tropopause.
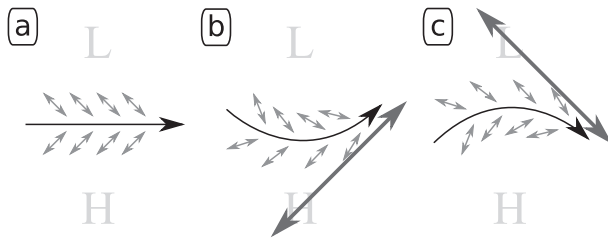
FIG. 10. Schematic of (a) straight and (b),(c) curved jet streams and the associated deformation angles. The small double arrows illustrate the deformation associated with wind shear perpendicular to the jet axis, and the large double arrows illustrate the additional deformation associated with the curvature of the jet axis.

On 4 November, two streamers of high PV are visible, indicating cyclonic wave breaking events (Fig. 9b; Thorncroft et al. 1993). The PV streamer close to the center of the map evolved from the short-wave trough discussed above, whereas the other over Newfoundland propagated into the depicted area. In both cases, the zonal collapse of the waves led to a collocation of the southward and northward jet streams, yielding strong deformation in between.

On 5 November, both PV streamers are cut off from the main jet stream (Fig. 9c). The band of strong deformation along the eastern streamer illustrates a continuing separation of the cutoff from the stratospheric PV reservoir. This separation is reflected in the γ-shaped deformation pattern, which we found to be a coherent feature in numerous cyclonic Rossby wave breaking events (not shown). Thus, this structure appears to be a characteristic of cyclonic wave breaking, suggesting that deformation plays a crucial role in the formation of the PV streamer going along with a wave breaking event. Further research will have to show whether deformation can be used to skillfully detect and classify wave breaking events into the Thorncroft et al. (1993) life cycles LC1 and LC2.

2) DEFORMATION IN IDEALIZED CURVED JET STREAMS

In the case study above, a distinct fish-bone pattern is evident in the orientation of the axis of dilatation with local asymmetries in the strength of deformation (Fig. 9). The deformation is stronger northward of ridges, like the one close to Greenland, or southward of troughs, like the one off the coast of Spain (Fig. 9a). Conversely, deformation is suppressed inside ridges and troughs.

This asymmetric pattern can be approximated by a superposition of the deformation along a straight jet and the deformation associated with its curvature. The fish-bone pattern is associated with the sign change of the wind shear at the jet axis (Fig. 10a), whereas a bend

of the jet yields additional deformation owing to its curvature (Fig. 1). Superposing the curvature-related deformation, indicated by the large double arrows in Figs. 10b and 10c, onto the fish-bone pattern yields the asymmetry in deformation. The total deformation increases where the large double arrow is within $\pm 45°$ of the fish-bone pattern, hence equatorward of the trough and poleward of the ridge.

The effect can be quantified by considering axisymmetric flow without a radial component. For such a flow, the total deformation is

$$\delta = |\delta_\times| = \left| -\frac{v}{r} + \frac{\partial v}{\partial r} \right|, \qquad (9)$$

where $v = v(r)$ is the azimuthal velocity component and r is the radius (see appendix for derivation). In the vicinity of a wind maximum of $v(r)$ at r_0, the term $-v/r$ is negative. The wind shear $\partial v/\partial r$ is positive for $r < r_0$ and negative for $r > r_0$, leading to suppressed deformation for $r < r_0$ and enhanced deformation for $r > r_0$.

3) COMPOSITES

The strongest deformation in the case study occurred in the two wave breaking episodes (Fig. 9). Accordingly, a composite of all cases with deformation above the 99th percentile for a similar location yields a similar deformation pattern (Fig. 11a). As in the case study, the region of strongest deformation is meridionally elongated and has a short-wave trough located closely to the southeast. In addition, there is an indication of the γ structure in the deformation and a ridge to the east. All these similarities indicate that Rossby wave breaking is the dominant contributor to this composite.

We only present results for one longitude in the Atlantic, as the results for other longitudes in the Atlantic, Pacific, or in the Southern Ocean are very similar (not shown). However, the composite strongly depends on the latitude of the selected location. For a location at higher latitudes, strong deformation events are associated with an anticyclone on the equatorward side (Fig. 11b). The anticyclone leads to an intensification of the jet at the location of the deformation maximum and thus an increased shear deformation as shown by the orientation of the axis of dilatation.

It is interesting to note that the same anticyclonic pattern with the zonally elongated deformation maximum is also evident for a composite of all cases with geopotential above the 99th percentile at relatively low latitudes (Fig. 12b). Both Figs. 11b and 12b are reminiscent of the analytic solution in Fig. 7 to the north of the spherical obstacle, where the accelerated flow leads to shearing deformation concentrated along the border of the obstacle.
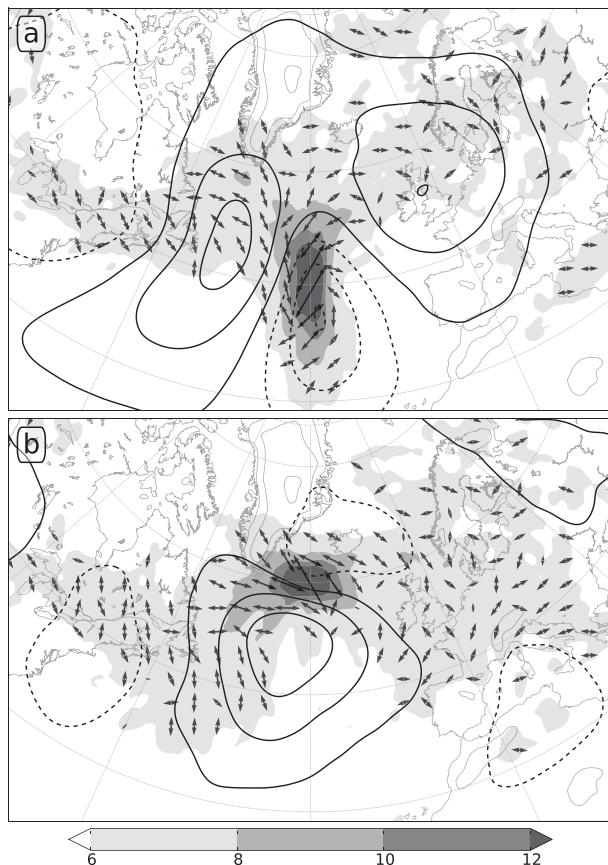
FIG. 11. Composite of cases with deformation above the 99th percentile in DJF at 300 hPa at (a) 45°N, 30°W and (b) 60°N, 30°W: shading and contours as in Fig. 5.
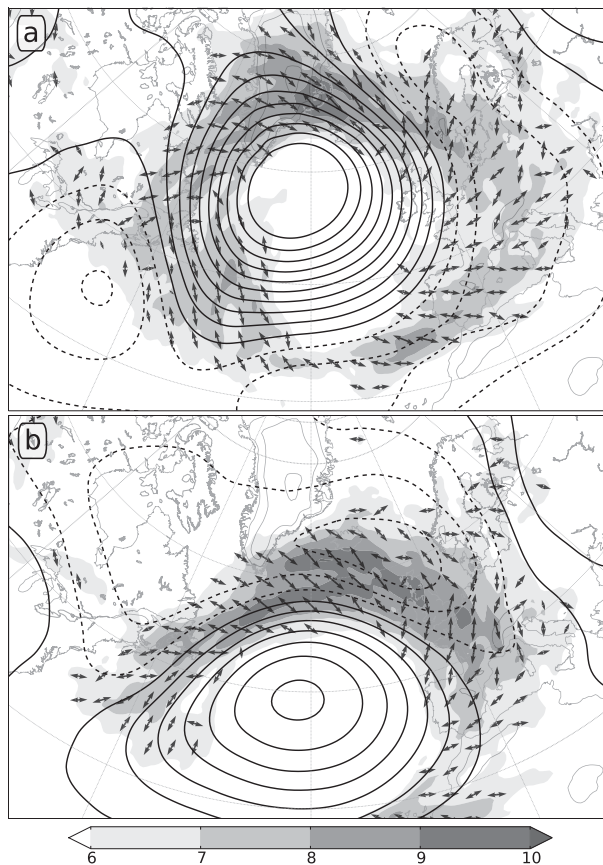

FIG. 12. Composite of cases with geopotential above the 99th percentile in DJF at 300 hPa at (a) 55°N, 30°W and (b) 40°N, 30°W: shading and contours as in Fig. 5.

The composite for the northerly geopotential anomaly in Fig. 12a corresponds closer to the analytic solution for blocking, as the belt of deformation around the block is almost axisymmetric, indicating that a block at this latitude not only deflects the flow to the north (as in Fig. 12b) but is also associated with flow splitting and, hence, a southerly and a northerly flow branch around the block. However, the belt does not coincide with the geopotential isolines but encompasses an almost deformation-free area to the southeast of the high. A comparison of Fig. 12a with the analytic solution (Fig. 7) in which the block is symmetrically surrounded by a belt of deformation suggests that the center of the block is, rather, located at the minimum in deformation than the maximum in geopotential.

On both sides of the blocking high in Fig. 12a, cyclonic anomalies with a shorter wavelength are present. The signature with two short-wave-length troughs on either side of the block close to the deformation maxima suggests that these are locations of preferred Rossby wave breaking. However, when comparing the deformation maxima with the composite dominated by Rossby wave

breaking (Fig. 11a), the signal in Fig. 12a is rather blurry. The signal and interpretation becomes much clearer when focusing on one specific blocking episode.

We have chosen the mean deformation for the second peak of the extreme heat wave in western Russia from 20 July to 10 August 2010 (Dole et al. 2011) as an illustrative example (Fig. 13). The heat wave is associated with a persistent blocking high, short-wavelength troughs on either side, and γ-shaped areas of intensified deformation. In this example, the deformation maxima on either side and the short-wave troughs are much sharper, closely resembling the Rossby wave breaking composite (Fig. 11a). The broad resemblance between this example and the composite in Fig. 12a supports the interpretation that the deformation maxima in the composite are preferred locations of Rossby wave breaking, even though the exact location of the breaking is more variable.

The coincidence of Rossby wave breaking and blocking supports previous theoretical (Swanson 2000) and observational (Berrisford et al. 2007; Altenhoff et al. 2008) work that argues for a close dynamical link
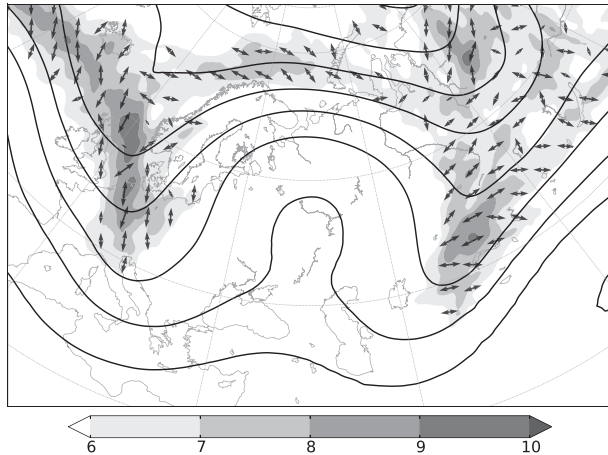
FIG. 13. Composite deformation for the period 20 Jul–10 Aug 2010, which covers the second peak of an extreme heat wave in western Russia. Shading as in Fig. 5; contours denote geopotential with a contour interval of $1000\,m^2\,s^{-2}$.
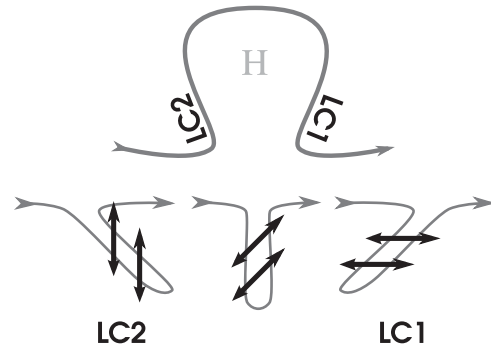

FIG. 14. Schematic of the relation between Rossby wave breaking and blocking. Double arrows indicate the orientation of the axis of dilatation. The meridionally oriented deformation associated with the preferred LC2 wave breaking upstream of the block supports the flow diversion around the block. Likewise, the zonally oriented deformation associated with LC1 wave breaking downstream is in line with confluence in the analytic solution (Fig. 7).

between wave breaking and blocking. Figure 13 illustrates that deformation provides a possible dynamic link owing to its important role in both filamentation of PV streamers and blocking. A potential mechanism by which Rossby wave breaking reinforces the block is illustrated in Fig. 14. The mechanism is based on the finding by Altenhoff et al. (2008) that cyclonic (LC2) and anticyclonic (LC1) wave breaking is prevalent upstream and downstream of the block, respectively. The corresponding orientation of the associated PV streamers results in an alignment of the deformation associated with the wave breaking and the deformation associated with the block itself. This alignment implies that wave breaking can act to strengthen the flow diversion around the block and hence contribute to the maintenance or intensification of the block. This finding is in accordance with previous work that found synoptic eddies to strengthen the block using the Hoskins et al. (1983) E-vector formalism (Shutts 1983; Hoskins and Sardeshmukh 1987; Woollings et al. 2008).

5. Summary and outlook

We demonstrated the potential of deformation as a diagnostic for large-scale atmospheric flow by investigating the value of deformation for better understanding (i) orographic blocking, (ii) dynamic blocking, and (iii) Rossby wave breaking. Our study indicates that deformation, indeed, provides a promising basis for objective detection algorithms for these three processes.

The observed deformation in the vicinity of orography in a case study of a cyclone interacting with Greenland agrees qualitatively well with the analytic solution for two-dimensional flow around a circular obstacle. Although there are other processes like shooting flows or tip jets that can lead to strong deformation close to orography, we demonstrated that those can be distinguished from blocking by either the location relative to the block or the orientation of the axis of dilatation. Furthermore, a composite analysis of strong deformation close to orography revealed that blocking is the dominant signal in these locations. The unambiguousness in the detection renders deformation a promising diagnostic to further analyze orographic blocking.

In contrast to traditional diagnostics for blocking, such as the mountain Froude number, deformation only relies on the local flow field and thus gives local information about the blocking intensity. As this information is also localized in the vertical, the vertical structure of deformation can hence give an indication about the depth of a blocked layer. Furthermore, the local blocking information can provide a basis for future work to better understand where, and how significantly, fronts are delayed by blocking orography, which is one of the most fundamental open questions regarding this interaction (Egger and Hoinka 1992).

In the upper troposphere, jet streams dominate the deformation field because of the large wind shear on either side of the jet axis. The sign change in the wind shear across the jet axis results in a characteristic fish-bone pattern in the axis of dilatation. When the wavelength of an undulation of the jet becomes short enough, jets of opposing directions meet. The shear between the opposing jets leads to the strongest deformation signatures in the upper troposphere. These signatures are associated with Rossby wave breaking, evident in the deformation fields through the typical γ-shaped deformation maximum.

These γ structures are also evident in composites for geopotential above the 99th percentile for locations within storm tracks. The co-occurrence of strong anticyclones and Rossby wave breaking supports earlier work that argued for a close dynamical link between blocking and wave breaking. Moreover, the deformation around a block also follows the analytic solution for flow around an obstacle. This, together with the finding of prevalent cyclonic (anticyclonic) Rossby wave breaking upstream (downstream) of the block by Altenhoff et al. (2008), suggests a potential mechanism establishing that link. Because of the cyclonic (anticyclonic) rotation, the shearing deformation associated with the breaking wave is aligned with the stretching deformation upstream (downstream) of the block, such that wave breaking can act to reinforce the flow diversion around the block.

Further research will show whether the deformation associated with blocking and wave breaking can be utilized for developing objective feature detection algorithms. The results in this study suggest that deformation could be used to (i) locally detect and quantify the strength of orographic blocking, (ii) identify the center of a dynamic block via a stationary minimum in deformation, (iii) detect and quantify the vigorousness of Rossby wave breaking events via the strength of deformation in the associated γ pattern, and (iv) detect the location of jet axes via the fish-bone pattern in the orientation of deformation.

APPENDIX

Deformation in Polar Coordinates

The wind vector in polar coordinates with (r, φ) is denoted (U, V), where U is the radial wind and V is the azimuthal wind. Then

$$\begin{pmatrix} u \\ v \end{pmatrix} = \begin{pmatrix} \cos\varphi & -\sin\varphi \\ \sin\varphi & \cos\varphi \end{pmatrix} \cdot \begin{pmatrix} U \\ V \end{pmatrix}, \qquad \text{(A1)}$$

and the deformation components result in

$$\delta_+ = 2\sin\varphi\cos\varphi\left(\frac{V}{r} - \frac{\partial V}{\partial r} - \frac{1}{r}\frac{\partial U}{\partial \varphi}\right)$$
$$+ (\sin^2\varphi - \cos^2\varphi)\left(\frac{U}{r} - \frac{\partial U}{\partial r} + \frac{1}{r}\frac{\partial V}{\partial \varphi}\right) \qquad \text{(A2)}$$

and

$$\delta_\times = -2\sin\varphi\cos\varphi\left(\frac{U}{r} - \frac{\partial U}{\partial r} + \frac{1}{r}\frac{\partial V}{\partial \varphi}\right)$$
$$+ (\sin^2\varphi - \cos^2\varphi)\left(\frac{V}{r} - \frac{\partial V}{\partial r} - \frac{1}{r}\frac{\partial U}{\partial \varphi}\right). \qquad \text{(A3)}$$

Equivalently to Eq. (6), total deformation can be calculated from a given streamfunction. In polar coordinates, the relation is

$$\delta = \sqrt{4\left(\frac{\psi_{r\varphi}}{r} - \frac{\psi_\varphi}{r^2}\right)^2 + \psi_{rr}^2 + \left(\frac{\psi_{\varphi\varphi}}{r^2} + \frac{\psi_r}{r}\right)^2 - 2\psi_{rr}\left(\frac{\psi_{\varphi\varphi}}{r^2} + \frac{\psi_r}{r}\right)}. \qquad \text{(A4)}$$

For an axisymmetric case with $U = 0$ and $V = V(r)$, the total deformation simplifies to

$$\delta = \left| -\frac{V}{r} + \frac{\partial V}{\partial r} \right|, \qquad \text{(A5)}$$

as can be validated easily along the x axis. There $\varphi = 0$ and, hence, $\delta_+ = 0$ and $|\delta_\times| = \delta$, as in Eq. (A5).

REFERENCES

Altenhoff, A. M., O. Martius, M. Croci-Maspoli, C. Schwierz, and H. C. Davies, 2008: Linkage of atmospheric blocks and synoptic-scale Rossby waves: A climatological analysis. *Tellus,* **60A,** 1053–1063, doi:10.1111/j.1600-0870.2008.00354.x.

Appenzeller, C., H. C. Davies, and W. A. Norton, 1996: Fragmentation of stratospheric intrusions. *J. Geophys. Res.,* **101,** 1435–1456, doi:10.1029/95JD02674.

Ball, F., 1956: The theory of strong katabatic winds. *Aust. J. Phys.,* **9,** 373–386, doi:10.1071/PH560373.

Batchelor, G. K., 1967: *An Introduction to Fluid Dynamics.* Cambridge University Press, 615 pp.

Berrisford, P., B. J. Hoskins, and E. Tyrlis, 2007: Blocking and Rossby wave breaking on the dynamical tropopause in the Southern Hemisphere. *J. Atmos. Sci.,* **64,** 2881–2898, doi:10.1175/JAS3984.1.

Bishop, C. H., and A. J. Thorpe, 1994: Frontal wave stability during moist deformation frontogenesis. Part I: Linear wave dynamics.

J. Atmos. Sci., **51,** 852–873, doi:10.1175/1520-0469(1994)051<0852: FWSDMD>2.0.CO;2.

Bjerknes, J., 1919: On the structure of moving cyclones. *Mon. Wea. Rev.,* **47,** 95–99, doi:10.1175/1520-0493(1919)47<95: OTSOMC>2.0.CO;2.

Black, R. X., and R. M. Dole, 2000: Storm tracks and barotropic deformation in climate models. *J. Climate,* **13,** 2712–2728, doi:10.1175/1520-0442(2000)013<2712:STABDI>2.0.CO;2.

Chaboureau, J.-P., and A. J. Thorpe, 1999: Frontogenesis and the development of secondary wave cyclones in FASTEX. *Quart. J. Roy. Meteor. Soc.,* **125,** 925–940, doi:10.1002/ qj.49712555509.

Charney, J. G., 1971: Geostrophic turbulence. *J. Atmos. Sci.,* **28,** 1087– 1095, doi:10.1175/1520-0469(1971)028<1087:GT>2.0.CO;2.

Davies, H. C., and A. M. Rossa, 1998: PV frontogenesis and upper-tropospheric fronts. *Mon. Wea. Rev.,* **126,** 1528–1539, doi:10.1175/1520-0493(1998)126<1528:PFAUTF>2.0.CO;2.

Dee, D. P., and Coauthors, 2011: The ERA-Interim reanalysis: Configuration and performance of the data assimilation system. *Quart. J. Roy. Meteor. Soc.,* **137,** 553–597, doi:10.1002/ qj.828.

Dole, R., and Coauthors, 2011: Was there a basis for anticipating the 2010 Russian heat wave? *Geophys. Res. Lett.,* **38,** L06702, doi:10.1029/2010GL046582.

Durran, D. R., 1986: Another look at downslope windstorms. Part I: The development of analogs to supercritical flow in an infinitely deep, continuously stratified fluid. *J. Atmos. Sci.,* **43,** 2527–2543, doi:10.1175/1520-0469(1986)043<2527: ALADWP>2.0.CO;2.

Eady, E., 1949: Long waves and cyclone waves. *Tellus,* **1A,** 33–52, doi:10.1111/j.2153-3490.1949.tb01265.x.

Egger, J., and K. Hoinka, 1992: Fronts and orography. *Meteor. Atmos. Phys.,* **48,** 3–36, doi:10.1007/BF01029557.

Harden, B. E., I. A. Renfrew, and G. N. Petersen, 2011: A climatology of wintertime barrier winds off southeast Greenland. *J. Climate,* **24,** 4701–4717, doi:10.1175/2011JCLI4113.1.

Hoskins, B. J., 1975: The geostrophic momentum approximation and the semi-geostrophic equations. *J. Atmos. Sci.,* **32,** 233–242, doi:10.1175/1520-0469(1975)032<0233:TGMAAT>2.0.CO;2.

——, and P. D. Sardeshmukh, 1987: A diagnostic study of the dynamics of the Northern Hemisphere winter of 1985–86. *Quart. J. Roy. Meteor. Soc.,* **113,** 759–778, doi:10.1002/qj.49711347705.

——, I. N. James, and G. H. White, 1983: The shape, propagation and mean-flow interaction of large-scale weather systems. *J. Atmos. Sci.,* **40,** 1595–1612, doi:10.1175/1520-0469(1983)040<1595: TSPAMF>2.0.CO;2.

——, M. E. McIntyre, and A. W. Robertson, 1985: On the use and significance of isentropic potential vorticity maps. *Quart. J. Roy. Meteor. Soc.,* **111,** 877–946, doi:10.1002/qj.49711147002.

Keyser, D., M. J. Reeder, and R. J. Reed, 1988: A generalization of Petterssen's frontogenesis function and its relation to the forcing of vertical motion. *Mon. Wea. Rev.,* **116,** 762–781, doi:10.1175/1520-0493(1988)116<0762:AGOPFF>2.0.CO;2.

Lamb, S. H., 1895: *Hydrodynamics.* Cambridge University Press, 604 pp.

LaPeyre, G., P. Klein, and B. Hua, 1999: Does the tracer gradient vector align with the strain eigenvectors in 2D turbulence? *Phys. Fluids,* **11,** 3729–3737, doi:10.1063/1.870234.

Massacand, A. C., H. Wernli, and H. C. Davies, 1998: Heavy precipitation on the alpine southside: An upper-level precursor. *Geophys. Res. Lett.,* **25,** 1435–1438, doi:10.1029/98GL50869.

McIntyre, M. E., and T. N. Palmer, 1983: Breaking planetary waves in the stratosphere. *Nature,* **305,** 593–600, doi:10.1038/305593a0.

Moore, G. W. K., and I. A. Renfrew, 2005: Tip jets and barrier winds: A QuikSCAT climatology of high wind speed events around Greenland. *J. Climate,* **18,** 3713–3725, doi:10.1175/ JCLI3455.1.

Okubo, A., 1970: Horizontal dispersion of floatable particles in the vicinity of velocity singularities such as convergences. *Deep-Sea Res. Oceanogr. Abstr.,* **17,** 445–454, doi:10.1016/ 0011-7471(70)90059-8.

Oruba, L., G. Lapeyre, and G. Rivire, 2013: On the poleward motion of midlatitude cyclones in a baroclinic meandering jet. *J. Atmos. Sci.,* **70,** 2629–2649, doi:10.1175/ JAS-D-12-0341.1.

Petersen, G. N., H. Ólafsson, and J. E. Kristjánsson, 2003: Flow in the lee of idealized mountains and Greenland. *J. Atmos. Sci.,* **60,** 2183–2195., doi:10.1175/1520-0469(2003)060<2183: FITLOI>2.0.CO;2.

——, I. A. Renfrew, and G. W. K. Moore, 2009: An overview of barrier winds off southeastern Greenland during the Greenland Flow Distortion experiment. *Quart. J. Roy. Meteor. Soc.,* **135,** 1950–1967, doi:10.1002/qj.455.

Petterssen, S., 1936: Contribution to the theory of frontogenesis. *Geofys. Publ.,* **11,** 5–27.

Renfrew, I. A., A. J. Thorpe, and C. H. Bishop, 1997: The role of the environmental flow in the development of secondary frontal cyclones. *Quart. J. Roy. Meteor. Soc.,* **123,** 1653–1675, doi:10.1002/qj.49712354210.

Ringler, T. D., and K. H. Cook, 1997: Factors controlling nonlinearity in mechanically forced stationary waves over orography. *J. Atmos. Sci.,* **54,** 2612–2629, doi: 10.1175/ 1520-0469(1997)054<2612:FCNIMF>2.0.CO;2.

Rivière, G., 2008: Barotropic regeneration of upper-level synoptic disturbances in different configurations of the zonal weather regime. *J. Atmos. Sci.,* **65,** 3159–3178, doi:10.1175/ 2008JAS2603.1.

——, 2009: Effect of latitudinal variations in low-level baroclinicity on eddy life cycles and upper-tropospheric wave-breaking processes. *J. Atmos. Sci.,* **66,** 1569–1592, doi:10.1175/ 2008JAS2919.1.

——, and A. Joly, 2006a: Role of the low-frequency deformation field on the explosive growth of extratropical cyclones at the jet exit. Part I: Barotropic critical region. *J. Atmos. Sci.,* **63,** 1965–1981, doi:10.1175/JAS3728.1.

——, and ——, 2006b: Role of the low-frequency deformation field on the explosive growth of extratropical cyclones at the jet exit. Part II: Baroclinic critical region. *J. Atmos. Sci.,* **63,** 1982– 1995, doi:10.1175/JAS3729.1.

——, and I. Orlanski, 2007: Characteristics of the Atlantic storm-track eddy activity and its relation with the North Atlantic Oscillation. *J. Atmos. Sci.,* **64,** 241–266, doi:10.1175/ JAS3850.1.

Sanders, F., 1986: Explosive cyclogenesis in the west-central North Atlantic Ocean, 1981–84. Part I: Composite structure and mean behavior. *Mon. Wea. Rev.,* **114,** 1781–1794, doi:10.1175/ 1520-0493(1986)114<1781:ECITWC>2.0.CO;2.

Shapiro, M. A., and D. A. Keyser, 1990: Fronts, jet streams, and the tropopause. NOAA Tech. Memo. ERL WPL 182, 75 pp.

Shutts, G. J., 1983: The propagation of eddies in diffluent jetstreams: Eddy vorticity forcing of 'blocking' flow fields. *Quart. J. Roy. Meteor. Soc.,* **109,** 737–761, doi:10.1002/ qj.49710946204.

Smith, R. B., 1979: The influence of mountains on the atmosphere. *Advances in Geophysics,* Vol. 21, Academic Press, 87–230, doi:10.1016/S0065-2687(08)60262-9.

Strong, C., and G. Magnusdottir, 2008: Tropospheric Rossby wave breaking and the NAO/NAM. *J. Atmos. Sci.,* **65,** 2861–2876, doi:10.1175/2008JAS2632.1.

Swanson, K. L., 2000: Stationary wave accumulation and the generation of low-frequency variability on zonally varying flows. *J. Atmos. Sci.,* **57,** 2262–2280, doi:10.1175/1520-0469(2000)057<2262:SWAATG>2.0.CO;2.

Thorncroft, C. D., B. J. Hoskins, and M. E. McIntyre, 1993: Two paradigms of baroclinic-wave life-cycle behaviour. *Quart. J. Roy. Meteor. Soc.,* **119,** 17–55, doi:10.1002/qj.49711950903.

Vallis, G. K., 2006: *Atmospheric and Oceanic Fluid Dynamics.* Cambridge University Press, 745 pp.

Vuorela, L. A., 1953: A synoptic study of deformation fields. *Tellus,* **5A,** 413–419, doi:10.1111/j.2153-3490.1953.tb01071.x.

Weiss, J., 1991: The dynamics of enstrophy transfer in two-dimensional hydrodynamics. *Physica D,* **48,** 273–294, doi:10.1016/0167-2789(91)90088-Q.

Wernli, H., and M. Sprenger, 2007: Identification and ERA-15 climatology of potential vorticity streamers and cutoffs near the extratropical tropopause. *J. Atmos. Sci.,* **64,** 1569–1586, doi:10.1175/JAS3912.1.

Woollings, T., B. Hoskins, M. Blackburn, and P. Berrisford, 2008: A new Rossby wavebreaking interpretation of the North Atlantic Oscillation. *J. Atmos. Sci.,* **65,** 609–626, doi:10.1175/2007JAS2347.1.